EUROPEAN RESPIRATORY *journal*

FLAGSHIP SCIENTIFIC JOURNAL OF ERS

Early View

Original research article

Dynamic Contrast Enhanced MRI for the Evaluation of Lung Perfusion in Idiopathic Pulmonary Fibrosis

Luis A. Torres, Kristine E. Lee, Gregory P. Barton, Andrew D. Hahn, Nathan Sandbo, Mark L. Schiebler, Sean B. Fain

Please cite this article as: Torres LA, Lee KE, Barton GP, *et al*. Dynamic Contrast Enhanced MRI for the Evaluation of Lung Perfusion in Idiopathic Pulmonary Fibrosis. *Eur Respir J* 2022; in press (https://doi.org/10.1183/13993003.02058-2021).

Dynamic Contrast Enhanced MRI for the Evaluation of Lung Perfusion in Idiopathic Pulmonary Fibrosis

Luis A. Torres, MS[1], Kristine E. Lee, MS[2], Gregory P. Barton, PhD[1], Andrew D. Hahn, PhD[1], Nathan Sandbo, MD[3], Mark L. Schiebler, MD[3,4], Sean B. Fain, PhD[1,4,5,6]

Affiliations:

[1]Department of Medical Physics, School of Medicine and Public Health, University of Wisconsin – Madison, Madison, WI
[2]Department of Biostatistics and Medical Informatics, School of Medicine and Public Health, University of Wisconsin – Madison, Madison, WI
[3]Department of Medicine, School of Medicine and Public Health, University of Wisconsin – Madison, Madison, WI
[4]Department of Radiology, School of Medicine and Public Health, University of Wisconsin – Madison, Madison, WI
[5]Department of Biomedical Engineering, College of Engineering, University of Wisconsin – Madison, Madison, WI
[6]Department of Radiology, Carver College of Medicine, University of Iowa – Iowa City, IA

Corresponding Author:

Sean Fain Ph.D. (sean-fain@uiowa.edu)
Professor and
Vice Chair of Research
Department of Radiology
University of Iowa
3939 John Pappajohn Pavilion
200 Hawkins Drive
Iowa City, IA 52242-1089

Summary

DCE-MRI quantitative perfusion and semi-quantitative transit time metrics identified regional deficits in IPF lung disease relative to healthy control subjects and in IPF progression.

Dynamic Contrast Enhanced MRI for the Evaluation of Lung Perfusion in Idiopathic Pulmonary Fibrosis

Abstract

Objectives: The objective of this work was to apply quantitative and semi-quantitative dynamic contrast enhanced MRI (DCE-MRI) methods to evaluate lung perfusion in idiopathic pulmonary fibrosis (IPF).

Materials and Methods: In this prospective trial 41 subjects, including healthy control (control) and IPF subjects, were studied using DCE-MRI at baseline. IPF subjects were then followed for 1 year, progressive IPF (IPF_{prog}) were distinguished from stable IPF (IPF_{stable}) subjects based on a decline in percent predicted FVC (FVC%p) or DLCO (DLCO%p) measured during followup visits. 35/41 subjects were retained for final baseline analysis at (control: N=15; IPF_{stable}: N = 14; IPF_{prog}: N=6). Seven measures and their coefficients of variation (CV) were derived using temporally resolved DCE-MRI. Two sets of global and regional comparisons were made: control vs IPF groups, and control vs IPF_{stable} vs IPF_{prog} groups, using linear regression analysis. Each measure was compared to FVC%p, DLCO%p, and the lung clearance index (LCI%p) using a Spearman rank correlation.

Results: DCE-MRI identified regional perfusion differences between control and IPF subjects using first moment transit time (FMTT), contrast uptake slope (SLOPE), and pulmonary blood flow (PBF) ($p \leq 0.05$), while global averages did not. FMTT was shorter for IPF_{prog} compared to both IPF_{stable} ($p = 0.004$) and control groups ($p = 0.023$). Correlations were observed between PBF CV and DLCO%p ($r_s = -0.48$, $p = 0.022$) and %LCI ($r_s = +0.47$, $p = 0.015$). Significant group differences were detected in age ($p < 0.001$), DLCO%p ($p < 0.001$), FVC%p ($p = 0.001$), and LCI%p ($p = 0.007$).

Conclusions: Global analysis obscures regional changes in pulmonary hemodynamics in IPF using DCE-MRI in IPF. Decreased FMTT may be a candidate marker for IPF progression.

INTRODUCTION

Idiopathic Pulmonary Fibrosis (IPF) is a fatal progressive disease affecting approximately 5 million people worldwide[1]. However, the pathology of IPF is difficult to characterize using conventional pulmonary function tests (PFTs), and disease progression is especially difficult to evaluate with current clinical tools. The standard of care for IPF is high-resolution computed tomography (HRCT) for initial diagnosis, and often this is accompanied by an invasive histological analysis. Longitudinal monitoring is performed using PFTs, including the change in forced vital capacity (FVC) and diffusing capacity of the lungs for carbon monoxide (DLCO). A significant drop in FVC and DLCO at 6-12 months has been shown to be moderately correlated with disease progression and mortality[2,3]. However, these are global lung measurements that might be insensitive to subtle regional changes in IPF. Additionally, significant progression of the disease must occur before changes in HRCT, FVC, and DLCO are detectable, reducing their overall clinical prognostic value[4]. Consequently, improved biomarkers for accurate monitoring and early detection of IPF progression are needed.

Pulmonary Magnetic Resonance Imaging (MRI) is a promising technique with the ability to provide longitudinal and regional information on pulmonary function[5]. Spatially resolved pulmonary perfusion is typically evaluated using dynamic contrast enhanced MRI (DCE-MRI), although various non-contrast methods are increasingly applied. DCE-MRI can provide quantitative and semi-quantitative measures and has been used to explore pulmonary hemodynamics in healthy and diseased subjects[6–10]. Despite the growing use of pulmonary contrast enhanced MRI, prior work in IPF is not extensive, and most research focuses on semi-quantitative analysis[11–15]. To our knowledge, there are no fully quantitative estimates of pulmonary hemodynamics in IPF using DCE-MRI techniques.

Quantitative measures based on indicator-dilution methods[16] provide physiological estimates of pulmonary blood flow (PBF), pulmonary blood volume (PBV), and mean transit

time (MTT)[17–19], while semi-quantitative measures are characteristics of the contrast enhancement time series such as contrast time-of-arrival (TOA), time-to-peak (TTP), first-moment-transit-time (FMTT), full width at half maximum (FWHM)[14], and wash-in slope (SLOPE)[10]. Advantages of more quantitative measures such as PBF, PBV, and MTT are offset by challenges in obtaining accurate measures of the arterial input function (AIF), increased computational complexity, and longer scan times required to obtain enough data to solve the ill-posed problem. Consequentially this leads to longer sustained breath-holds and increased potential for motion corruption. This makes accurate quantitation especially difficult in severely diseased or non-compliant subjects (e.g., pediatric) who have a significant imaging failure rate. Alternatively, semi-quantitative measures are simpler to compute and require fewer temporal phases. This can improve the chances of successful imaging, albeit without the advantages of consistent hemodynamic physiological interpretation.

The objective of this work was to develop quantitative and semi-quantitative DCE-MRI methods for application in IPF. We hypothesized DCE-MRI could be used to detect global and regional perfusion differences between IPF and healthy aging volunteers. In an exploratory analysis we also followed IPF subjects for 1 year clinically to monitor progression; we hypothesized there would be differences in perfusion measures in a progressive subgroup of IPF (IPF_{prog}) compared to a stable subgroup of IPF (IPF_{stable}) and to healthy aging volunteers. We tested these hypotheses using a repeated measures linear regression analysis to adjust for demographic and technical factors found to be significant covariates. Furthermore, we hypothesized our measures of hemodynamics would correlate with clinical PFTs used to monitor IPF progression, specifically FVC, DLCO and the Lung Clearance index (LCI), a measure of ventilation heterogeneity.

Methods

Study Population

Our HIPAA-compliant and IRB approved (UW IRB 2013-0266 and UW IRB 2014-1572) prospective study included 41 subjects imaged longitudinally (2-4 visits) using DCE-MRI. Written and informed consent was obtained from all subjects. Healthy subjects were included for study if > 18 years of age, current non-smoker, and no history of cancer or heart disease. The Healthy subject population was deliberately enriched for individuals > 50 years and 65% male sex to better match the age and sex distribution of the recruited IPF population. IPF subjects required age >18 years with clinical diagnosis of IPF and no recent exacerbations. Exclusion criteria consisted of MRI contraindication, pregnancy/lactation, or any medical condition that could interfere with the ability to comply with the protocol. IPF_{prog} were distinguished from IPF_{stable} subjects by a >10% decline in percent predicted FVC (FVC%p) or a >15% decline in percent predicted DLCO (DLCO%p) 1 year after baseline PFT measures. For this feasibility study we limit analysis to the first visit passing quality control for each subject and leave longitudinal analysis for a subsequent report. Subject attrition during the study is summarized in **Supplemental Table 1**. Specifically, two stable IPF subjects withdrew during their first visit due to claustrophobia, while technical failure occurred in 4 more subjects (1 healthy, 3 progressive IPF) due to either loss of breath-hold during the scan or delayed arrival of contrast agent leading to truncation of the contrast kinetic curve; these subject scans were omitted from analysis based on the number of frames of wash-out data obtained in the AIF. Each image series was visually inspected and excluded if there was a loss of breath-hold. If a subject's initial baseline visit failed quality control, a subsequent passing baseline visit was used in its place. A total of 35 of 41 subjects were included for analysis (healthy control: N=15, 5 males, 56.3±14.2 years, IPF_{stable}: N = 14, 12 males, 69.9±9.3 years, IPF_{prog}: N=6, 5 males, 75.7±4.4 years). Descriptive

statistics and intragroup comparisons for the 35 subjects included in the analysis can be seen in **Table 1**.

Acquisition and Reconstruction Protocol

Subjects were scanned while supine at end-expiratory breath hold. Contrast injection was performed using a dose of 0.05 mmol/kg of gadobenate dimeglumine (Gd-BOPTA, Multihance; Bracco Imaging) at 4 mL/s followed by a 35 mL saline flush to approximate a linear relationship between signal intensity and contrast concentration in the lung parenchyma[20].

Due to hardware upgrades during the study, subjects were imaged at both 1.5T and 3T field strengths. DCE pulmonary perfusion scans were acquired using 3D spoiled gradient-echo sequences. Similar sampling schemes were used for time-resolved acquisition at each field strength, including a research pulse sequence, "interleaved Variable Density" (IVD) [21] at 1.5T (Signa HDxt, GE Healthcare), and a commercial pulse sequence, "Differential Subsampling with Cartesian Ordering" (DISCO, GE Healthcare)[22] at 3T (Discovery MR750, GE Healthcare). Both sequences were acquired with full chest coverage i.e., FOV = 40 (S/I) × 28 (A/P) × 40 (L/R) cm^3 and a parallel acceleration factor of 2x2. Spatial (4 mm isotropic) and temporal resolutions (nominally 1 s) were matched for each protocol. Other relevant scan parameters can be found in **Table 2**.

Post Processing

Semi-Automatic Lung Segmentation and Arterial Input Function Selection

Segmentation was performed using a combination of ITK-SNAP[23] (v3.8) and Python (Python Software Foundation, https://www.python.org/, v3.6). Consecutively acquired morphological images were used to semi-automatically segment the perfusion datasets similar to Kohlmann et al[24]. Each lung was segmented into 6 regions by volume. An example can be seen in **supplementary figure 1**. To remove potential user error in AIF selection, we implemented an automated method where we apply successive image processing steps to our

dynamic images to gradually isolate the pulmonary trunk and pinpoint its branching point[25]. Additionally, a cross-correlation analysis with the AIF was performed to suppress large vessel influence[26]. A visualization of these steps is included in **supplementary figure 2** and a more detailed description of these methods are included in the supplementary text. Because subjects with extreme motion are excluded from this analysis, we do not apply additional image registration on the DCE timeseries.

Quantitative and Semi-Quantitative Measures

PFT measures were performed with a MasterScreen PFT system using reference values computed as recommended by the Global Lung Function Initiative[27]. The computation of each measure was performed using MATLAB (MathWorks, Natick, MA, R2018b). Supplementary **figure 3** outlines the workflow for computing quantitative and semi-quantitative measures as well as example parametric maps in a healthy subject. Voxel-wise relative enhancement was computed via subtraction of and normalization to the baseline mask signal. Using the principles of indicator dilution theory, we can solve for PBF, PBV, and MTT. Specifically, the following relationships hold under a few basic assumptions[16]:

$$\mathrm{C(t)} = \mathrm{PBF}[\mathrm{R(t)} \otimes \mathrm{AIF}] \quad \textbf{Eq. 1}$$

$$\mathrm{PBV} = \frac{\int C(t)dt}{\int AIF(t)dt} \quad \textbf{Eq. 2}$$

$$\mathrm{MTT} = \frac{PBV}{PBF}\,. \quad \textbf{Eq. 3}$$

Here $\mathrm{C(t)}$ and $\mathrm{R(t)}$ are the concentration at the volume of interest and the tissue residue function at time t, respectively. The main task here is to deconvolve Eq. 1 to solve for $PBF \times \mathrm{R(t)}$. This is an ill-posed problem that requires regularization to reach physiologically plausible solutions[19,28]. Once $PBF \times \mathrm{R(t)}$ is computed we solve for PBV and MTT using Eq. 2 and Eq.3. In this work PBF, PBV, and MTT were estimated by solving a least squares deconvolution problem

with Tikhonov regularization[16,29,30]. Details on the deconvolution procedure are included in the supplemental text. Semi-quantitative parameters are conceptually simpler to compute. The contrast kinetic curves were smoothed using a second order Savitsky-Golay filter with a window size of 5 frames. Each time-series was up-sampled by a factor of 2 using linear interpolation. TOA and TTP were defined as the timepoint at which the signal enhancement curve reaches 20% and 100% of its peak value, respectively. The TTP of the AIF was subtracted from TOA and TTP to remove potential bolus injection timing differences across subjects. Finally, SLOPE and FMTT were calculated as follows:

$$\mathrm{SLOPE} = \frac{\mathrm{S(TTP)} - \mathrm{S(TOA)}}{TTP - TOA} \quad \textbf{Eq. 4}$$

$$\mathrm{FMTT} = \frac{\int S(t) * t dt}{\int S(t) dt} \quad \textbf{Eq. 5}$$

Here $\mathrm{S(TTP)}$ is the peak signal and $\mathrm{S(TOA)}$ is the baseline signal at TOA. For a visual example of how these parameters are associated with the contrast kinetics see **supplementary figure 4**.

Statistical analysis

Comparison of characteristics between controls, IPF_{stable} and IPF_{prog} was done using non-parametric tests (Wilcoxon Rank sum for numeric variables and Fisher's Exact for categorical variables) for every pairwise comparison (IPF_{stable} to controls, IPF_{prog} to controls and IPF_{stable} to IPF_{prog}). A Bonferroni p-value correction using n=3 comparisons was applied to account for multiple-comparisons bias.

We evaluated relationships to each DCE measure on both the whole lung and a region-specific level. Linear regression models were used to evaluate the relationship of cohort to the whole lung DCE measure. For region-specific DCE measures, each subject has 12 measures

consisting of 6 regions (3 anterior and 3 posterior) for both the right and left lung. Repeated measures linear regression was performed where correlations between observations within a subject were modeled using an unstructured covariance matrix. Potential simplifications of the variance-covariance structure were assessed using Akaike's Information Criterion. The most parsimonious model considering cohort, region (6 level) and lung (left or right) as well as potential interactions was identified and was similar for most measures. The final parameter estimates were obtained using the Restricted Maximum Likelihood. Model effects for the 6 level region and 2 level "side" (left or right lung) were evaluated and only the region effect improved the fit and was retained for the final models. Thus, the final models for region-specific DCE measures included terms for cohort, region and the interaction between cohort and region.

For each DCE measure, we separately evaluated the mean in the appropriate area (whole lung or region-specific) and their CV (mean/sd for the whole lung or for the specific region). All models adjusted for sex (2 level: female vs male), age (continuous) and field strength (2 level: 1.5T vs 3T). Cohort was evaluated separately as a 3-level factor with controls (as the referent group) and IPF_{stable} and IPF_{prog}, but also as a 2-level factor with the IPF_{stable} and IPF_{prog} considered together as "IPF". Normality of each DCE measure was evaluated visually and because each measure has a different range they were rescaled to a z-score for comparisons.

Least-squares means and 95% confidence intervals with adjustment for age, sex and field strength were estimated for the relevant cohort and region levels. For the whole lung analysis this consists of cohort, and for region-specific analysis this consists of cohort and region interaction. The whole lung analysis reports the p-value for the cohort comparison. The region-specific analysis reports the p-value for the interaction term as well as the joint likelihood ratio test to get the marginal "overall cohort" (cohort + cohort*region) and "overall region" (region + region*cohort) effects, which represent overall impact of cohort or region.

Spearman correlations were evaluated to compare each DCE-MRI measure with FVC%p, DLCO%p, and LCI%p. The FVC%p, DLCO%p, and LCI%p were measured prior to the DCE-MRI scans, on the same day of each visit, using a MasterScreen PFT system and reference values were computed as recommended by the Global Lung Function Initiative[27]. All analyses were done in SAS (SAS Institute, Inc., Cary NC, v9.4) and R (R Core Team, 2021).

Results

Global lung averages did not differ significantly between IPF and control subjects, even after adjusting for age, sex, and field strength (**Figure 1a**); however, regional comparisons showed significant differences between IPF and healthy control subjects for mean PBF, SLOPE and FMTT measures ($p \leq 0.05$; **Figure 2**). For each metric we saw significant cohort, lung region, and interaction effects. No statistical differences were found between left and right lungs; thus, the left and right lungs were grouped into apical, middle, and basal lung regions for both the posterior and anterior. Similar variation between lung regions were seen in all measures irrespective of cohort. Regional heterogeneity patterns were also captured across lung regions and cohorts using the CV in which significant cohort differences were observed for PBF, TTP, and FMTT ($p \leq 0.05$; **Figure 3**).

A subset of exemplary parametric maps in two healthy and two IPF subjects are highlighted in **Figure 4**. We observed whole lung and regional abnormalities in IPF relative to healthy subjects, including increased heterogeneity (CV) of perfusion measures. In healthy control subjects the expected gravity-dependent anterior to posterior gradient pattern predominates, while in IPF subjects additional inter-patient and regional spatial variations in severity of perfusion abnormalities were typical. For example, in IPF subject 1 reduced global perfusion is observed, while in IPF subject 2 regional variation in perfusion between the apical

and basal lung regions are prominent compared to healthy subjects. A more complete set of parametric maps can be seen in **supplementary figure 5.**

Further exploratory comparisons of control vs IPF_{prog} and IPF_{stable} found global and regional differences in semi-quantitative perfusion measures. The global mean FMTT was *shorter* in IPF_{prog} relative to healthy ($p = 0.023$) and IPF_{stable} groups ($p = 0.004$; **Figure 1b**). No other measures showed global differences between groups. Regional analysis for these cohorts showed similarly significant differences for control vs IPF_{stable} for FMTT ($p = 0.030$), control vs IPF_{prog} for FMTT ($p = 0.036$), where FMTT was *shorter* in IPF_{prog}. Of potential importance for discriminating progression from stable disease, TTP ($p = 0.032$) and FMTT ($p < 0.001$) were both shorter in IPF_{prog} vs IPF_{stable}. Similarly, the FMTT CV differed within regions for IPF_{prog} vs controls ($p=0.034$), and importantly, the FMTT CV differed between IPF_{prog} and IPF_{stable} ($p = 0.002$, **Figure 6**).

Finally, the regional heterogeneity of perfusion measures as measured by CV was significantly correlated to PFTs. There was mild/moderate correlation between the PBF CV vs DLCO%p ($r_s = -0.48$, $p = 0.022$), and LCI%p ($r_s=+0.47$, $p = 0.015$. No other perfusion measures were found to correlate to PFTs. Significant group differences were detected in age, DLCO%p FVC%p and LCI%p ($p < 0.05$).

Discussion

DCE-MRI identified regional perfusion differences between control subjects and IPF lung disease using FMTT, SLOPE, and PBF, although global lung averages did not. Heterogeneity in these measures using the CV was also greater in IPF. This suggests global analysis obscures regional changes in pulmonary hemodynamics and highlights the need for regional imaging approaches. Generally, we see increased FMTT, and decreased PBF and SLOPE in IPF relative to control subjects, consistent with reports of vascular pruning and overall reduction of vascular density in severely fibrotic areas[31–34]. The increased CV of FMTT, TTP, and PBF

represent increased regional heterogeneity in IPF relative to healthy control subjects, also consistent with reports of spatially heterogenous vascular remodeling in IPF[33]

There were significant regional variations and trends in all DCE measures consistent with gravitational dependence and previously published works[17,35]. This pattern is likely related to the supine patient orientation within the MRI scanner and residual anatomic and physiologic effects of upright posture. Additionally, we found larger group discrepancies in the posterior-basal portions of the lungs in all measures and the CV supported more pronounced perfusion differences in these areas, consistent with typical manifestations of IPF[36,37].

Interestingly, in our exploratory analysis we observed a global decrease in FMTT between IPF_{prog} and both the IPF_{stable} and healthy control groups, but no differences were observed between the control and IPF_{stable} groups suggesting decreased FMTT may be a candidate marker for progression. One explanation for the shorter FMTT in the IPF_{prog} group is increased regional heterogeneity of vascular density and central vessel diameter due to vascular pruning and remodeling. Ebina et al. found that acute exacerbation, a severe and often fatal adverse event associated with rapid progression, was associated with increased and dilated capillaries[31]. Similarly, a CT based vessel analysis found increased vessel size to be highly predictive of mortality[38]. IPF manifests as a heterogeneous fibrotic injury and is predominantly found in the basal and peripheral portions of the lungs[36,37] and previous work with DCE-MRI indicates that changes can be detected easier in these areas[14,15]. It is thought that repetitive environmental microinjuries to interstitial and vascular tissue induce abnormal healing responses which result in heterogeneous interstitial and vascular remodeling[36,39]. Early results had seemingly conflicting reports of reduced/increased vascular density in IPF. However, this was later reconciled with studies on the spatial heterogeneity of the disease and evidence supports that severely fibrotic areas demonstrate a reduction in vascular density, while adjacent tissues display an increase in vascularization[31]. Although the mechanism and causality of the increased vascularization and fibrogenesis is unclear, some authors suggest it is a precursor to

fibrosis[40,41]. Additionally, increased vascularization and vessel diameter has also been implicated in acute exacerbations in IPF, which lead to rapid progression of fibrosis and result in higher mortality rates[31]. Accurate, regional evaluation of pulmonary microvasculature could provide insight into the pathogenic process of IPF, and these exploratory results warrant further study in a larger population to determine if FMTT remains a possible predictor of progression and to inform on the possible underlying mechanism driving shorter FMTT.

With regards to comparisons to PFTs, including FVC%p, DLCO%p and LCI%p, we observed somewhat unanticipated findings of non-significant and universally weak correlation associations with the mean values of all perfusion measures. Although there were moderate correlations of DLCO%p and LCI%p with measures of perfusion heterogeneity, no correlations of any perfusion measures were observed with FVC%p. The explanation for this pattern probably lies in heterogeneous compensatory increases in pulmonary perfusion to offset lung function decline. Weatherly et al.[14] report similar results in which DLCO%p was not correlated with the contrast curve full width at half max (FWHM), yet DLCO%p was correlated with the FWHM interquartile range (IQR), a measure of regional heterogeneity. This heterogeneity is one reason why IPF is difficult to evaluate and further emphasizes the value of spatially resolved functional lung imaging in this disease.

Some clarifications should be made with respect to previous work. Weatherly et al. show significant longitudinal increases in global FWHM over 6-months in IPF subjects. In this work we focus on establishing baseline differences between a healthy cohort and IPF subjects with clinical outcomes of progression after 1 year. Given our focus on clinical progression, these results are not mutually exclusive and evaluate different aspects of DCE measures in the context of IPF. The present work demonstrates improved discriminatory power by leveraging the regional information contained within DCE-MRI, and we expect that this improvement will translate to longitudinal monitoring of DCE measures in IPF as well. We also note that Weatherly et al. demonstrated a non-statistically significant increase in FWHM in a small subset

of non-survivors. This is partly in contrast to our findings, which indicate a decrease in FMTT using a different definition of progression. We suspect that the results are not directly comparable due to the different classification of “progressors” vs “non-survivors” as well as inherent differences between FWHM and FMTT as measures of transit time.

Finally, when comparing global pulmonary function test measures, FVC%p, DLCO%p and LCI%p all show significant differences across groups, specifically between control and IPFprog. Of the perfusion measures, only FMTT demonstrated significant global differences. This suggests that either global perfusion measures are not as sensitive as FVC%p, DLCO%p and LCI%p, or that global perfusion measures are measuring fundamentally different aspects of the disease. However, we emphasize that, unlike global measures of either perfusion or pulmonary function tests, regional FMTT uniquely distinguished between stable IPF and IPF progression.

Limitations

This study has some limitations. First is the small sample size, especially in the IPF_{prog} subgroup, that necessarily makes the exploration of perfusion markers of progression speculative and prone to selection bias. In this study we also had an unbalanced dataset with respect to of age, sex, and field strength. Our cohorts have statistically different age distributions, which could affect our measures as perfusion tends to decrease with increased age. With respect to field strength differences, tissue T1 relaxation times will be longer at 3T than at 1.5T which will also systematically reduce the SNR in our measurements. Although our models account for these biases and imbalances it is possible that bias remains even after statistical adjustments due to insufficient overlap between groups.

Second, although we use a small, optimized, contrast dose to target the pseudo-linear relationship between contrast dose and signal amplitude, it is possible to have systematic

biases in our quantitative parameters due to this signal saturation effect. We did not observe any noticeable saturation effects and our estimates are comparable to those found in the literature for hemodynamics measured using DCE-MRI and SPECT/PET.

Conclusion

In this work we demonstrate that global analysis obscures regional changes in pulmonary hemodynamics in IPF using DCE-MRI. Quantitative PBF and semi-quantitative FMTT perfusion also clearly delineated healthy subjects from IPF patients. Moreover, decreased FMTT was found in the subset of IPF patients who progressed and should be investigated further as a candidate marker for IPF progression in a larger study population. We also observed significant correlations of CV's in perfusion measures with DLCO%p and LCI%p as surrogates for vascular heterogeneity. Notably, FVC%p, DLCO%p and LCI%p all demonstrated significant differences between healthy and IPF, although they did not distinguish between stable and progressive IPF. In total, these results suggest DCE-MRI is a promising tool for identifying early vascular remodeling of the capillary networks in IPF, which could serve as an early predictor of rapid progression.

Conflict of Interest

M.L.S reports grant funding from the National Heart, Lung, and Blood Institute (NHLBI SARPIII - RFA-HL-11-018 and SARP IV 4P01HL088594-09, R01 HL080414) and ownership of Elucida Oncology Inc., Elucida Medical Inc., Healthmyne Inc., Stemina Biomarker Discovery Inc., and X-Vax, Inc. S.B.F reports grant funding from NHLBI (NHLBI R01HL126771, NHLBI RO1 HL146689), GE Healthcare, American Lung Association, as well as compensation from Caladarius Biosciences, Polarean PLC, and Sanofi/Regeneron. All other authors have nothing to disclose.

References

1. Meltzer EB, Noble PW. Idiopathic pulmonary fibrosis. *Orphanet Journal of Rare Diseases* 2008;3:8.

2. Bois RM du, Weycker D, Albera C, et al. Forced vital capacity in patients with idiopathic pulmonary fibrosis: test properties and minimal clinically important difference. *Am J Respir Crit Care Med* 2011;184(12):1382–1389.

3. Doubková M, Švancara J, Svoboda M, et al. EMPIRE Registry, Czech Part: Impact of demographics, pulmonary function and HRCT on survival and clinical course in idiopathic pulmonary fibrosis. *Clin Respir J* 2018;12(4):1526–1535.

4. Davies JC, Cunningham S, Alton EWFW, Innes JA. Lung clearance index in CF: a sensitive marker of lung disease severity. *Thorax* 2008;63(2):96–97.

5. Torres L, Kammerman J, Hahn AD, et al. "Structure-Function Imaging of Lung Disease Using Ultrashort Echo Time MRI." *Academic Radiology* 2019;26(3):431–441.

6. Barton GP, Torres LA, Goss KN, Eldridge MW, Fain SB. Pulmonary Microvascular-Changes in Adult Survivors of Prematurity: Utility of DCE MRI. *Am J Respir Crit Care Med* [Internet] 2020 [cited 2020 Nov 2];Available from: https://www.atsjournals.org/doi/abs/10.1164/rccm.202002-0344LE

7. Maxien D, Ingrisch M, Meinel F, Reiser M, Dietrich O, Nikolaou K. Quantification of Pulmonary Perfusion with Free-Breathing Dynamic Contrast-Enhanced MRI – A Pilot Study in Healthy Volunteers. *RöFo - Fortschritte auf dem Gebiet der Röntgenstrahlen und der bildgebenden Verfahren* 2013;185(12):1175–1181.

8. Ley S, Ley-Zaporozhan J. Pulmonary perfusion imaging using MRI: clinical application. *Insights Imaging* 2011;3(1):61–71.

9. Ohno Y, Koyama H, Matsumoto K, et al. Dynamic MR perfusion imaging: capability for quantitative assessment of disease extent and prediction of outcome for patients with acute pulmonary thromboembolism. *J Magn Reson Imaging* 2010;31(5):1081–1090.

10. Hueper K, Parikh M, Prince MR, et al. Quantitative and Semi-quantitative Measures of Regional Pulmonary Parenchymal Perfusion by Magnetic Resonance Imaging and their Relationships to Global Lung Perfusion and Lung Diffusing Capacity – The MESA COPD Study. *Invest Radiol* 2013;48(4):223–230.

11. Sergiacomi G, Bolacchi F, Cadioli M, et al. Combined Pulmonary Fibrosis and Emphysema: 3D Time-resolved MR Angiographic Evaluation of Pulmonary Arterial Mean Transit Time and Time to Peak Enhancement. *Radiology* 2010;254(2):601–608.

12. Mirsadraee S, Tse M, Kershaw L, et al. T1 characteristics of interstitial pulmonary fibrosis on 3T MRI—a predictor of early interstitial change? *Quant Imaging Med Surg* 2016;6(1):42–49.

13. Lavelle LP, Brady D, McEvoy S, et al. Pulmonary fibrosis: tissue characterization using late-enhanced MRI compared with unenhanced anatomic high-resolution CT. *Diagn Interv Radiol* 2017;23(2):106–111.

14. Weatherley ND, Eaden JA, Hughes PJC, et al. Quantification of pulmonary perfusion in idiopathic pulmonary fibrosis with first pass dynamic contrast-enhanced perfusion MRI. *Thorax* 2021;76(2):144–151.

15. Montesi S, Zhou IY, Digumarthy S, Seethamraju RT, Caravan P. DYNAMIC CONTRAST-ENHANCED MRI TO ASSESS THE MICROVASCULATURE IN IPF. *Chest* 2019;156(4, Supplement):A2268.

16. Meier P, Zierler KL. On the Theory of the Indicator-Dilution Method for Measurement of Blood Flow and Volume. *Journal of Applied Physiology* 1954;6(12):731–744.

17. Ohno Y, Hatabu H, Murase K, et al. Quantitative assessment of regional pulmonary perfusion in the entire lung using three-dimensional ultrafast dynamic contrast-enhanced magnetic resonance imaging: Preliminary experience in 40 subjects. *J Magn Reson Imaging* 2004;20(3):353–365.

18. Hopkins SR, Levin DL, Emami K, et al. Advances in magnetic resonance imaging of lung physiology. *J Appl Physiol (1985)* 2007;102(3):1244–1254.

19. Østergaard L, Weisskoff RM, Chesler DA, Gyldensted C, Rosen BR. High resolution measurement of cerebral blood flow using intravascular tracer bolus passages. Part I: Mathematical approach and statistical analysis. *Magn Reson Med* 1996;36(5):715–725.

20. Neeb D, Kunz RP, Ley S, et al. Quantification of pulmonary blood flow (PBF): Validation of perfusion MRI and nonlinear contrast agent (CA) dose correction with H 215O positron emission tomography (PET). *Magn Reson Med* 2009;62(2):476–487.

21. Wang K, Schiebler ML, Francois CJ, et al. Pulmonary perfusion MRI using interleaved variable density sampling and HighlY constrained cartesian reconstruction (HYCR): Pulmonary Perfusion Using IVD HYCR. *Journal of Magnetic Resonance Imaging* 2013;38(3):751–756.

22. Saranathan M, Rettmann DW, Hargreaves BA, Clarke SE, Vasanawala SS. DIfferential Subsampling with Cartesian Ordering (DISCO): a High Spatio-temporal Resolution Dixon Imaging Sequence for Multiphasic Contrast Enhanced Abdominal Imaging. *J Magn Reson Imaging* 2012;35(6):1484–1492.

23. Yushkevich PA, Piven J, Hazlett HC, et al. User-guided 3D active contour segmentation of anatomical structures: Significantly improved efficiency and reliability. *NeuroImage* 2006;31(3):1116–1128.

24. Kohlmann P, Strehlow J, Jobst B, et al. Automatic lung segmentation method for MRI-based lung perfusion studies of patients with chronic obstructive pulmonary disease. *Int J CARS* 2015;10(4):403–417.

25. Kohlmann P, Laue H, Krass S, Peitgen H-O. Fully-Automatic Determination of the Arterial Input Function for Dynamic Contrast-Enhanced Pulmonary MR Imaging. In: MIUA. 2011.

26. Risse F, Kuder TA, Kauczor H-U, Semmler W, Fink C. Suppression of pulmonary vasculature in lung perfusion MRI using correlation analysis. *Eur Radiol* 2009;19(11):2569.

27. Stanojevic S, Grham B, Cooper B, Thompson B, Carter K, Hall G. Global lung function initiative: Reference equations for the transfer factor for carbon monoxide (TLCO). *European Respiratory Journal* [Internet] 2016 [cited 2020 Nov 8];48(suppl 60). Available from: https://erj.ersjournals.com/content/48/suppl_60/OA283

28. Østergaard L. Principles of cerebral perfusion imaging by bolus tracking. *J Magn Reson Imaging* 2005;22(6):710–717.

29. Sourbron S, Luypaert R, Morhard D, Seelos K, Reiser M, Peller M. Deconvolution of bolus-tracking data: a comparison of discretization methods. *Phys Med Biol* 2007;52(22):6761.

30. Bell LC, Wang K, Del Rio AM, Grist T, Fain SB, Nagle SK. Comparison of Models and Contrast Agents for Improved Signal and Signal Linearity in Dynamic Contrast-Enhanced Pulmonary MRI. *Invest Radiol* 2015;50(3):174–178.

31. Ebina M. Pathognomonic remodeling of blood and lymphatic capillaries in idiopathic pulmonary fibrosis. *Respiratory Investigation* 2017;55(1):2–9.

32. Ebina M, Shimizukawa M, Shibata N, et al. Heterogeneous Increase in CD34-positive Alveolar Capillaries in Idiopathic Pulmonary Fibrosis. *Am J Respir Crit Care Med* 2004;169(11):1203–1208.

33. Mlika M, Bacha S, Braham E, El Mezni F. The inter-connection between fibrosis and microvascular remodeling in idiopathic pulmonary fibrosis: Reality or just a phenomenon. *Respiratory Medicine Case Reports* 2016;17:30–33.

34. Farkas L, Kolb M. Pulmonary Microcirculation in Interstitial Lung Disease. *Proc Am Thorac Soc* 2011;8(6):516–521.

35. Levin DL, Chen Q, Zhang M, Edelman RR, Hatabu H. Evaluation of regional pulmonary perfusion using ultrafast magnetic resonance imaging. *Magn Reson Med* 2001;46(1):166–171.

36. Plantier L, Cazes A, Dinh-Xuan A-T, Bancal C, Marchand-Adam S, Crestani B. Physiology of the lung in idiopathic pulmonary fibrosis. *Eur Respir Rev* 2018;27(147):170062.

37. Lederer DJ, Martinez FJ. Idiopathic Pulmonary Fibrosis. *New England Journal of Medicine* 2018;378(19):1811–1823.

38. Jacob J, Bartholmai BJ, Rajagopalan S, et al. Mortality prediction in idiopathic pulmonary fibrosis: evaluation of computer-based CT analysis with conventional severity measures. *European Respiratory Journal* [Internet] 2017 [cited 2021 Mar 27];49(1). Available from: https://erj.ersjournals.com/content/49/1/1601011

39. Parra ER, David YR, Costa LRS da, et al. Heterogeneous Remodeling of Lung Vessels in Idiopathic Pulmonary Fibrosis. *Lung* 2005;183(4):291–300.

40. Puxeddu E, Cavalli F, Pezzuto G, Teodori E, Rogliani P. Impact of pulmonary vascular volume on mortality in IPF: is it time to reconsider the role of vasculature in disease pathogenesis and progression? *European Respiratory Journal* [Internet] 2017 [cited 2021 Mar 18];49(2). Available from: https://erj.ersjournals.com/content/49/2/1602345

41. Probst CK, Montesi SB, Medoff BD, Shea BS, Knipe RS. Vascular permeability in the fibrotic lung. *European Respiratory Journal* [Internet] 2020 [cited 2021 Mar 19];56(1). Available from: https://erj-ersjournals-com.ezproxy.library.wisc.edu/content/56/1/1900100

Figure Captions

Figure 1: Whole-lung linear regression model results for cohort means (left) and CVs (right) of FMTT, TTP, SLOPE, and PBF. a) demonstrates expected means in healthy controls (blue) and a combined IPF cohort (red) while b) demonstrates the means in healthy controls (blue), stable IPF (red), and progressive IPF (purple).

Figure 2: Regional repeated measure regression model results for the mean values of FMTT (top left), TTP (top right), SLOPE (bottom left), and PBF (bottom right) in healthy control (blue) and combined IPF (red) subjects.

Figure 3: Regional repeated measure regression model results for the coefficients of variation (CV) of FMTT (top left), TTP (top right), SLOPE (bottom left), and PBF (bottom right) in healthy control (blue) and IPF (red) subjects.

Figure 4: A subset of exemplary parametric maps of pulmonary blood flow (PBF), SLOPE, and FMTT in two healthy and two IPF subjects. For PBF and SLOPE, green and red colors indicate more and less perfusion, respectively. For FMTT, blue and red indicate faster and slower transit times. We observe whole lung and regional abnormalities in IPF relative to age matched healthy subjects. Regional heterogeneity of perfusion measures is observed in all subjects. An anterior to posterior gradient is observed in addition to reduced perfusion in the distal portions of the lungs. In IPF subjects, inter-patient as well as regional variation in severity is observed.

Figure 5: Exploratory regional repeated measure regression model results for the mean values of FMTT (top left), TTP (top right), SLOPE (bottom left), and PBF (bottom right) in healthy control, stable (IPF_{stable}), and progressive subjects (IPF_{prog}).

Figure 6: Exploratory regional repeated measure model results for the coefficients of variation (CV) of FMTT (top left), TTP (top right), SLOPE (bottom left), and PBF (bottom right) in healthy control, stable (IPF_{stable}), and progressive participants (IPF_{prog}) participants.

	Table 1. Population Characteristics					
	Control (N=15)	**IPF_{stable} (N=14)**	**IPF_{prog} (N=6)**	**[1]Control vs IPF_{stable} P-value**	**[1]Control vs IPF_{prog} P-value**	**[1]IPF_{stable} vs IPF_{prog} P-value**
3.0 T N (%)	3 (20.0)	6 (42.9)	3 (50.0)	0.735	0.872	1.000
Female N (%)	10 (66.7)	2 (14.3)	1 (16.7)	**0.023**	0.190	1.000
Age (Years) Median (IQR)	63.0 (51.5, 66.0)	69.0 (64.0, 74.0)	75.5 (72.5, 79.3)	**0.020**	**0.002**	0.320
DLCO%P Median (IQR) N (%)	94.0 (72.8, 105.5) 8 (53.0)	57.0 (54.0, 67.0) 13 (92.8)	46.0 (45.0, 50.0) 5 (83.3)	**0.006**	**0.013**	0.090
FVC%P Median (IQR) N (%)	105.0 (94.0,109.0) 9 (60.0)	85.5 (75.8, 92.8) 14 (100.0)	66.5 (57.5, 74.8) 6 (100.0)	**0.050**	**0.005**	0.062
LCI%P Median (IQR) N (%)	7.4 (7.2, 7.6) 8 (53.0)	7.7 (7.5, 7.9) 12 (75.0)	8.0 (7.9, 8.125) 4 (66.7)	0.068	**0.025**	0.385
PBF (ml/100ml/min) Median (IQR)	189.0 (142.6, 214.3)	155.8 (134.1,193.0)	203.47 (185.0, 216.2)	0.978	1.000	0.447
PBV (ml/100ml) Median (IQR)	16.4 (12.4, 18.3)	13.7 (13.1, 14.2)	14.7 (12.1, 15.8)	1.000	1.000	1.000
MTT (s) Median (IQR)	5.6 (5.3, 5.8)	5.2 (4.6, 6.8)	5.3 (5.2, 5.7)	1.000	1.000	1.000
SLOPE (a.u.) Median (IQR)	1.3 (1.2, 1.9)	1.3 (0.8, 1.8)	1.3 (1.1, 1.4)	0.716	1.000	1.000
FMTT (s) Median (IQR)	12.9 (12.4, 13.3)	13.2 (12.9, 16.3)	13.1 (12.2, 13.4)	0.231	1.000	0.796
TOA (s) Median (IQR)	0.7 (0.2, 0.9)	0.9 (0.7, 1.5)	0.6 (0.3, 0.8)	0.181	1.000	0.323
TTP (s) Median (IQR)	5.2 (4.8, 5.7)	5.9 (5.5, 8.3)	5.8 (5.3, 6.2)	0.108	1.000	1.000

[1] Numerical values tested using Wilcoxon Rank Sum test, Categorical values tested using Fischer's Exact Test, P-values adjusted via the Bonferroni method using three comparisons.

Table 2. Imaging Parameters		
	[1]IVD	[2]DISCO
[3]TR (ms)	2.2	2.3
[4]TE (ms)	0.7	0.7
Flip Angle (°)	25	30
[5]FOV (mm^3)	400x280x400	400x280x400
Acquisition Matrix	100x70x400	100x70x400
Acquired voxel size (mm^3)	4.0x4.0x4.0	4.0x4.0x4.0
Acceleration factor (R)	2	2
Acquired Time Frames	23	27
Scan Length (s)	21	31
Bandwidth (kHz)	125	125
Number of subjects	23	12

[1] Interleaved Variable Density
[2] Differential Subsampling with Cartesian Ordering
[3] Repetition Time
[4] Echo Time
[5] Field of View

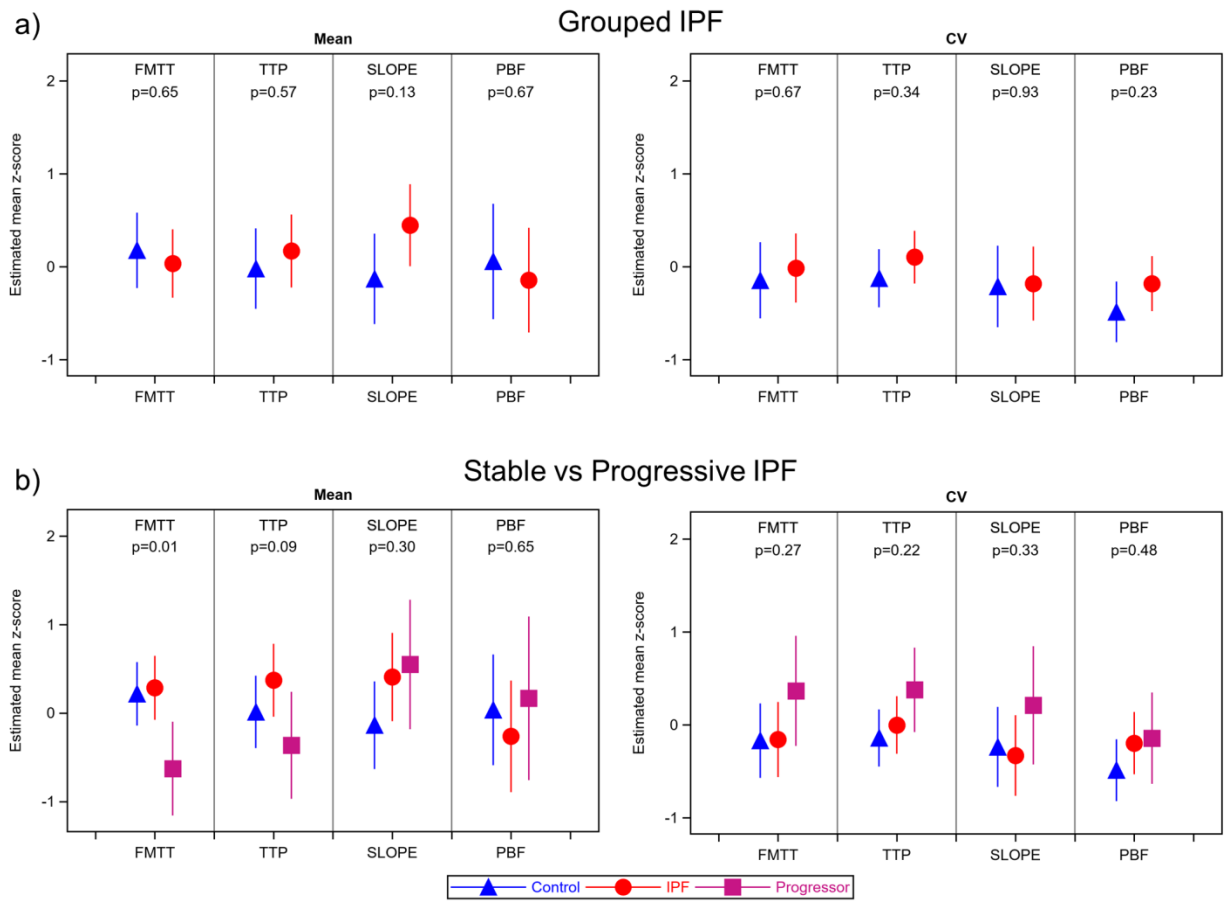
a)
Grouped IPF
Mean
CV
FMTT
p=0.65
TTP
p=0.57
SLOPE
p=0.13
PBF
p=0.67
FMTT
p=0.67
TTP
p=0.34
SLOPE
p=0.93
PBF
p=0.23
Estimated mean z-score
2
1
0
-1
FMTT
TTP
SLOPE
PBF
b)
Stable vs Progressive IPF
Mean
CV
FMTT
p=0.01
TTP
p=0.09
SLOPE
p=0.30
PBF
p=0.65
FMTT
p=0.27
TTP
p=0.22
SLOPE
p=0.33
PBF
p=0.48
Estimated mean z-score
Control
IPF
Progressor

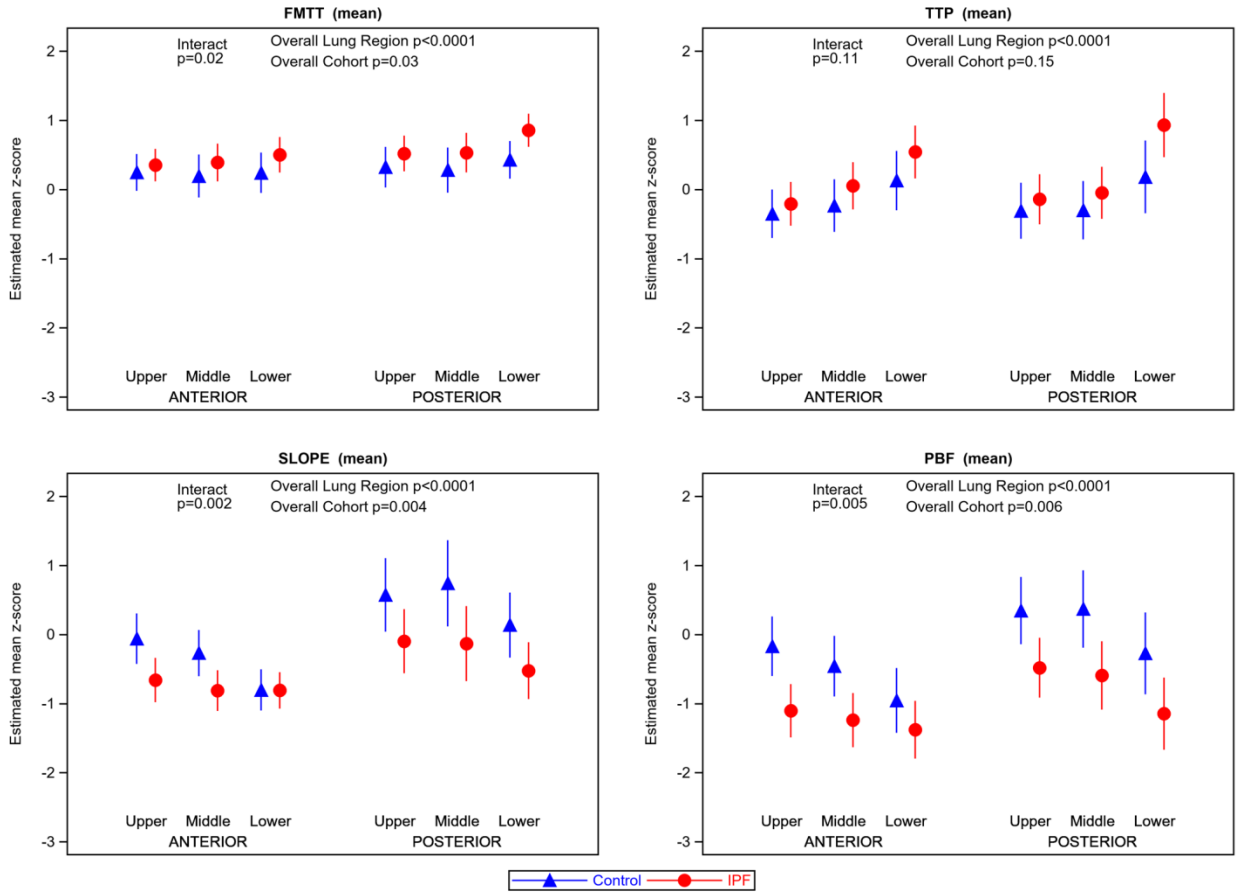
FMTT (mean)
Interact p=0.02
Overall Lung Region p<0.0001
Overall Cohort p=0.03
TTP (mean)
Interact p=0.11
Overall Lung Region p<0.0001
Overall Cohort p=0.15
SLOPE (mean)
Interact p=0.002
Overall Lung Region p<0.0001
Overall Cohort p=0.004
PBF (mean)
Interact p=0.005
Overall Lung Region p<0.0001
Overall Cohort p=0.006
Estimated mean z-score
2
1
0
-1
-2
-3
Upper Middle Lower
ANTERIOR
Upper Middle Lower
POSTERIOR
Control
IPF

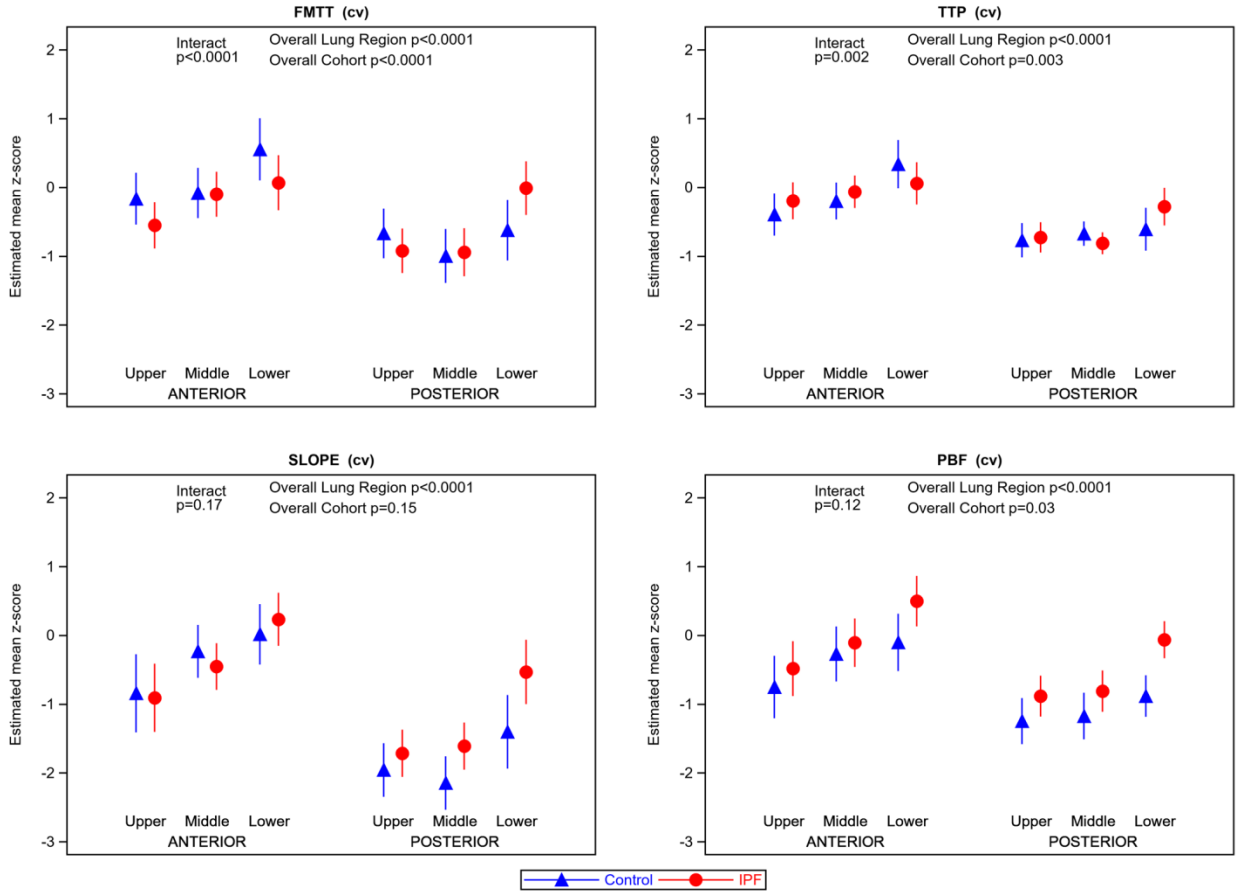
FMTT (cv)
Interact p<0.0001
Overall Lung Region p<0.0001
Overall Cohort p<0.0001
TTP (cv)
Interact p=0.002
Overall Lung Region p<0.0001
Overall Cohort p=0.003
SLOPE (cv)
Interact p=0.17
Overall Lung Region p<0.0001
Overall Cohort p=0.15
PBF (cv)
Interact p=0.12
Overall Lung Region p<0.0001
Overall Cohort p=0.03
Estimated mean z-score
2
1
0
-1
-2
-3
Upper Middle Lower
ANTERIOR
Upper Middle Lower
POSTERIOR
Control
IPF

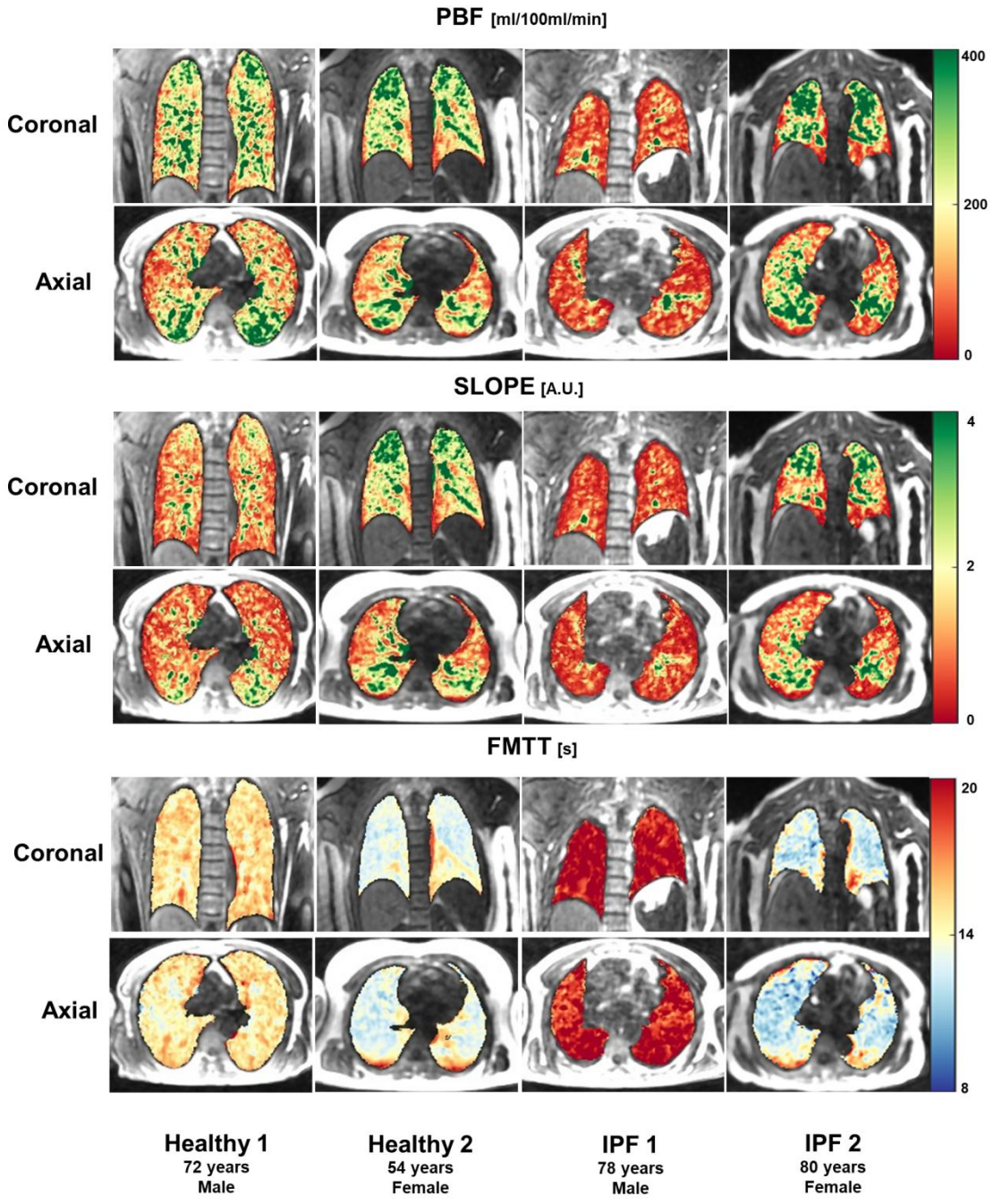
PBF [ml/100ml/min]
Coronal
Axial
400
200
0
SLOPE [A.U.]
Coronal
Axial
4
2
0
FMTT [s]
Coronal
Axial
20
14
8
Healthy 1
72 years
Male
Healthy 2
54 years
Female
IPF 1
78 years
Male
IPF 2
80 years
Female

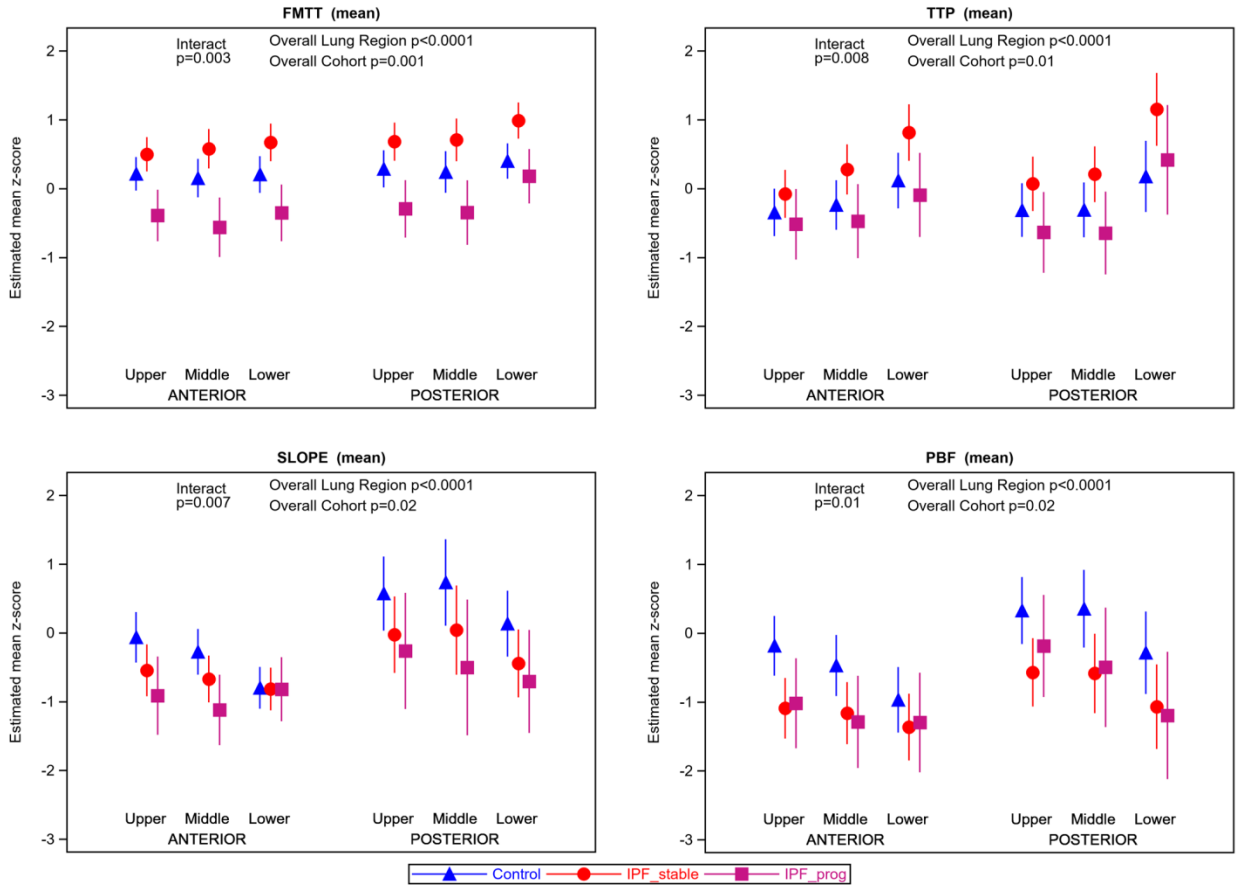
FMTT (mean)
Interact p=0.003
Overall Lung Region p<0.0001
Overall Cohort p=0.001
TTP (mean)
Interact p=0.008
Overall Lung Region p<0.0001
Overall Cohort p=0.01
SLOPE (mean)
Interact p=0.007
Overall Lung Region p<0.0001
Overall Cohort p=0.02
PBF (mean)
Interact p=0.01
Overall Lung Region p<0.0001
Overall Cohort p=0.02
Estimated mean z-score
2
1
0
-1
-2
-3
Upper Middle Lower
ANTERIOR
Upper Middle Lower
POSTERIOR
Control
IPF_stable
IPF_prog

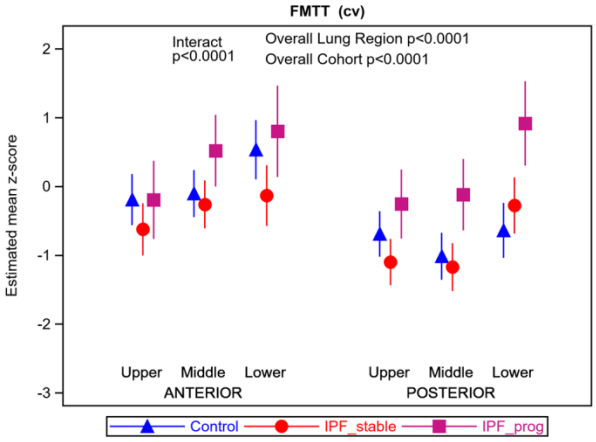
FMTT (cv)
Interact p<0.0001
Overall Lung Region p<0.0001
Overall Cohort p<0.0001
Estimated mean z-score
2
1
0
-1
-2
-3
Upper Middle Lower
ANTERIOR
Upper Middle Lower
POSTERIOR
Control
IPF_stable
IPF_prog

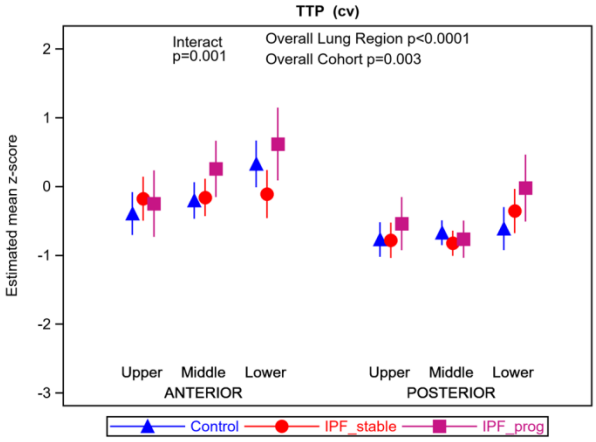
TTP (cv)
Interact p=0.001
Overall Lung Region p<0.0001
Overall Cohort p=0.003
Estimated mean z-score
2
1
0
-1
-2
-3
Upper Middle Lower
ANTERIOR
Upper Middle Lower
POSTERIOR
Control
IPF_stable
IPF_prog

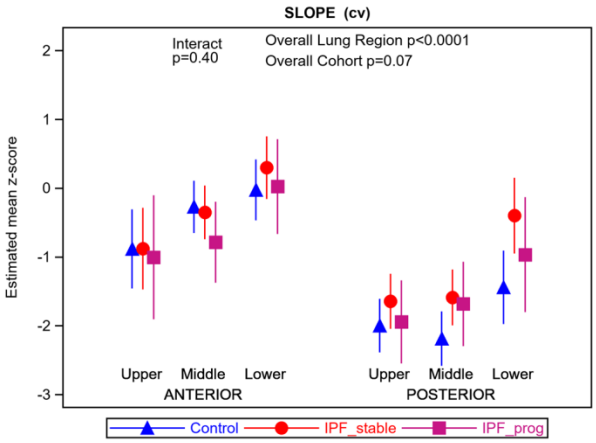
SLOPE (cv)
Interact p=0.40
Overall Lung Region p<0.0001
Overall Cohort p=0.07
Estimated mean z-score
2
1
0
-1
-2
-3
Upper Middle Lower
ANTERIOR
Upper Middle Lower
POSTERIOR
Control
IPF_stable
IPF_prog

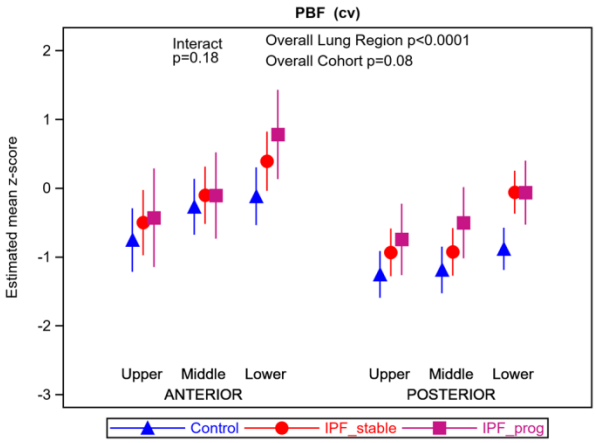
PBF (cv)
Interact p=0.18
Overall Lung Region p<0.0001
Overall Cohort p=0.08
Estimated mean z-score
2
1
0
-1
-2
-3
Upper Middle Lower
ANTERIOR
Upper Middle Lower
POSTERIOR
Control
IPF_stable
IPF_prog

Supplementary Text

Automated Segmentation

Consecutively morphological images were acquired using optimized 3D center-out radial ultra-short echo time sequence[1] (UTE, TE/TR=0.08/3.14 ms, 90,000 spokes). The morphological images were segmented at a whole lung level using a 2.5D deep convolutional neural network for healthy participants[2]. Since the network has not been trained for IPF subjects, a user-guided active contouring approach for participants with IPF [3]. The resulting lung segmentations were further split into 6 regions per lung. Each lung was split into three sections of equal volume in the superior-inferior direction, then each subsection was further divided into two equal volume sections in the anterior-posterior direction. This resulted in 12 regions per subject. An example segmentation can be seen in **Supplemental Figure 1**. The morphological images were then registered to the initial frame of the DCE scan using a B-spline deformable registration approach using the Advanced Normalization Toolkit, and the transforms were applied to the segmentation[4,5]

Automated Arterial Input Function Selection

We first remove a large majority of background voxels by applying a median filter, computing a temporal maximum intensity projection (tMIP) and thresholding based on 25% of the maximum signal intensity in order to keep a segmentation largely composed of the heart, large arteries, and veins. This segmentation is then cleaned using morphological operations and the pulmonary artery is separated from the aorta by performing a histogram analysis on the TTP in

these regions combined with Otsu thresholding. This results in a segmentation that consists of the right ventricle and the pulmonary artery, which is subsequently skeletonized. Finally, a graph analysis is used to pinpoint the branching point and a cube of 50 voxels surrounding that point to define the AIF region of interest (ROI). **Supplementary Figure 2** outlines the workflow for AIF selection.

Deconvolution Solution

After discretization of the AIF, we can write equation 1 as:

$$\mathbf{Ax} = \mathbf{b} \qquad \textbf{Eq. 1}$$

In this form $\mathbf{A}$ is the discretized AIF, $\mathbf{b}$ contains the elements of $\mathrm{C(t)}$, and $\mathbf{x}$ corresponds to $PBF \times \mathrm{R(t)}$. In this work we used a block circulant discretization to reduce bias from tracer arrival delay[6]. Specifically, we solve the following minimization problem for each voxel:

$$\mathbf{arg\,min} \left\| \mathbf{Ax} - \mathbf{b} \right\|_2^2 + \lambda \left\| \mathbf{x} \right\|_2^2. \qquad \textbf{Eq. 2}$$

In Eq. 5, λ is the regularization value that trades off the smoothness of the solution with the data consistency. This system has an analytical solution which can be implemented efficiently via the singular value decomposition (SVD). The regularization parameter λ was selected using an L-curve criterion optimization for each voxel to estimate the best tradeoff between the error and the smoothness of the solution[7].

Model Interpretation

In this work we apply linear regression and repeated measures models to evaluate various effects while adjusting for multiple factors (age, sex, and field strength). For regional analysis,

overall cohort, overall region, and cohort/region interaction effects are reported. Specifically, in our regional analysis figures we report three p-values for each measure: “Overall Lung Region”, “Overall Cohort”, and “Interact”, which for simplicity I will label P1, P2, and P3. These p-values can take the following main permutations for each metric:

1. If P1 – Significant, P2 – Non-significant, P3 – Non-significant, this implies significant differences between lung regions, but no differences in cohort.

2. If P1 – Significant, P2 – Significant, P3 – Non-significant, this implies significant differences between lung regions, significant differences between cohorts, but not driven by any specific lung region. In other words, all lung regions trend similarly.

3. If P1 – Significant, P2 – Significant, P3 –Significant, this implies significant differences between lung regions, significant differences between cohorts, AND significant differences between cohorts in a specific lung region. In contrast to 2, this indicates that one or more regions trend significantly higher or lower than the consensus of the rest of the regions.

We note that a significant interaction indicates a distinct cohort/region effect, however like typical ANOVA analysis, it does not identify which region is responsible for the significant differences. Further statistical analysis is required to determine which regions are driving the interaction term.

References

1. Johnson KM, Fain SB, Schiebler ML, Nagle S. Optimized 3D ultrashort echo time pulmonary MRI. *Magn Reson Med* 2013;70(5):1241–1250.

2. Zha W, Fain SB, Schiebler ML, Evans MD, Nagle SK, Liu F. Deep convolutional neural networks with multiplane consensus labeling for lung function quantification using UTE proton MRI. *J Magn Reson Imaging* 2019;50(4):1169–1181.

3. Yushkevich PA, Piven J, Hazlett HC, et al. User-guided 3D active contour segmentation of anatomical structures: Significantly improved efficiency and reliability. *NeuroImage* 2006;31(3):1116–1128.

4. Tustison NJ, Avants BB. Explicit B-spline regularization in diffeomorphic image registration. *Front Neuroinform* [Internet] 2013;7. Available from: https://www.ncbi.nlm.nih.gov/pmc/articles/PMC3870320/

5. Tustison NJ, Cook PA, Klein A, et al. Large-scale evaluation of ANTs and FreeSurfer cortical thickness measurements. *NeuroImage* 2014;99:166–179.

6. Wu O, Østergaard L, Weisskoff RM, Benner T, Rosen BR, Sorensen AG. Tracer arrival timing-insensitive technique for estimating flow in MR perfusion-weighted imaging using singular value decomposition with a block-circulant deconvolution matrix. *Magn Reson Med* 2003;50(1):164–174.

7. Sourbron S, Dujardin M, Makkat S, Luypaert R. Pixel-by-pixel deconvolution of bolus-tracking data: optimization and implementation. *Physics in Medicine and Biology* 2007;52(2):429–447.

Tables

Supplementary Table 1. Study Attrition

Retention Stages	**Total N (%)**
Total IPF Recruitment	41 (100%)
↳Subjects with DCE-MRI	39 (95%)
↳Passing QC for **at least 1 baseline** visit	35 (85%)

Figures

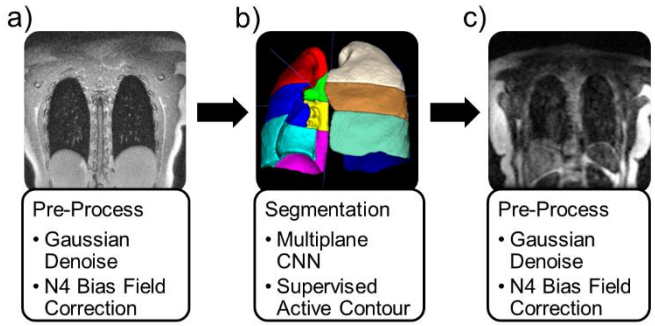

Supplemental Figure 1: Image Segmentation workflow. a) Consecutively acquired morphological image is denoised, bias field corrected, and semi-automatically segmented. b) The lung segmentation is then split into posterior and anterior, apical, middle, and basal lung regions by volume. c) The initial mask for DCE-MRI images is denoised, bias field corrected, and then the morphological image is deformably registered to this mask. The subsequent deformation field is applied to the lung segmentation as a final step.

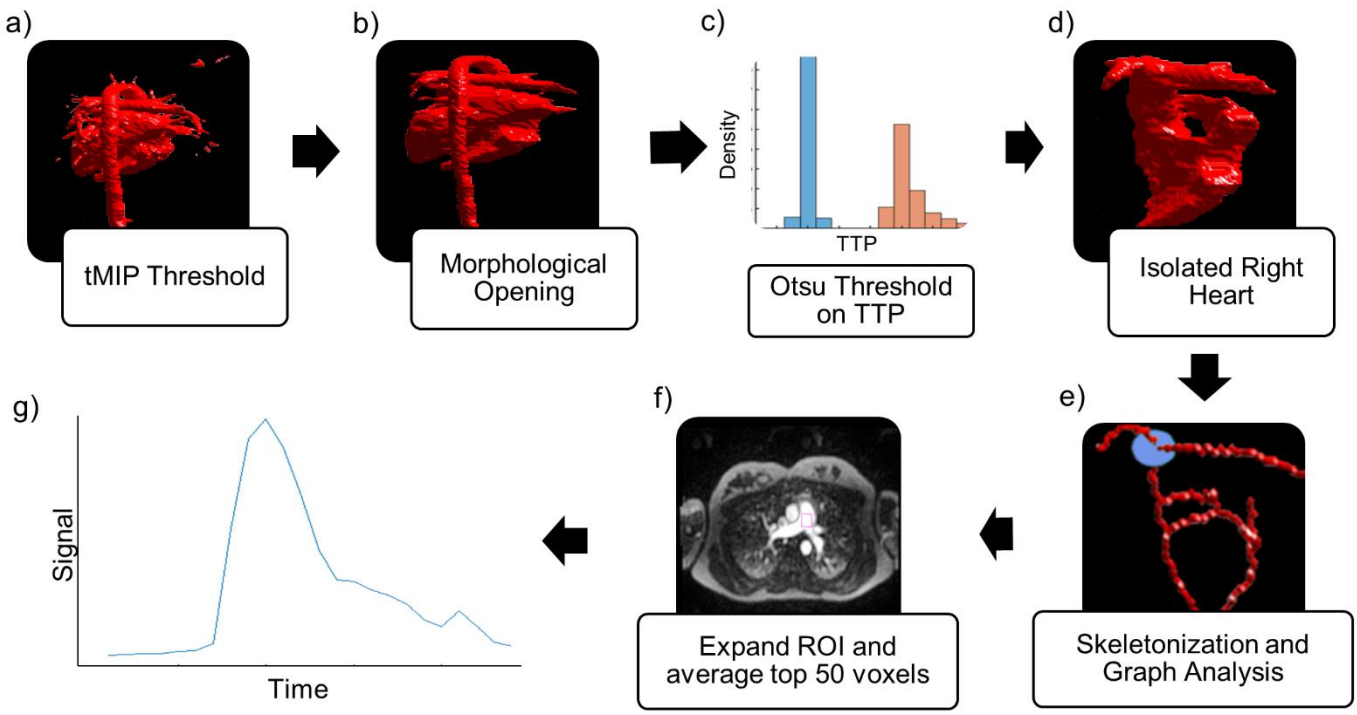

Supplemental Figure 2. Arterial Input function selection workflow. We first remove a large majority of background voxels by thresholding a temporal maximum intensity projection (a). This segmentation is then cleaned using morphological opening, closing, and erosion operations (b) and the pulmonary artery is separated from the aorta by performing a histogram analysis (c). This results in a segmentation that consists of the right ventricle and the pulmonary artery (d). This segmentation is subsequently skeletonized, and a graph analysis is used to pinpoint the branching point (e). A cube of 50 voxels surrounding that point to define the AIF region of interest (f). The mean values of the region of interest are used to compute the AIF (g).

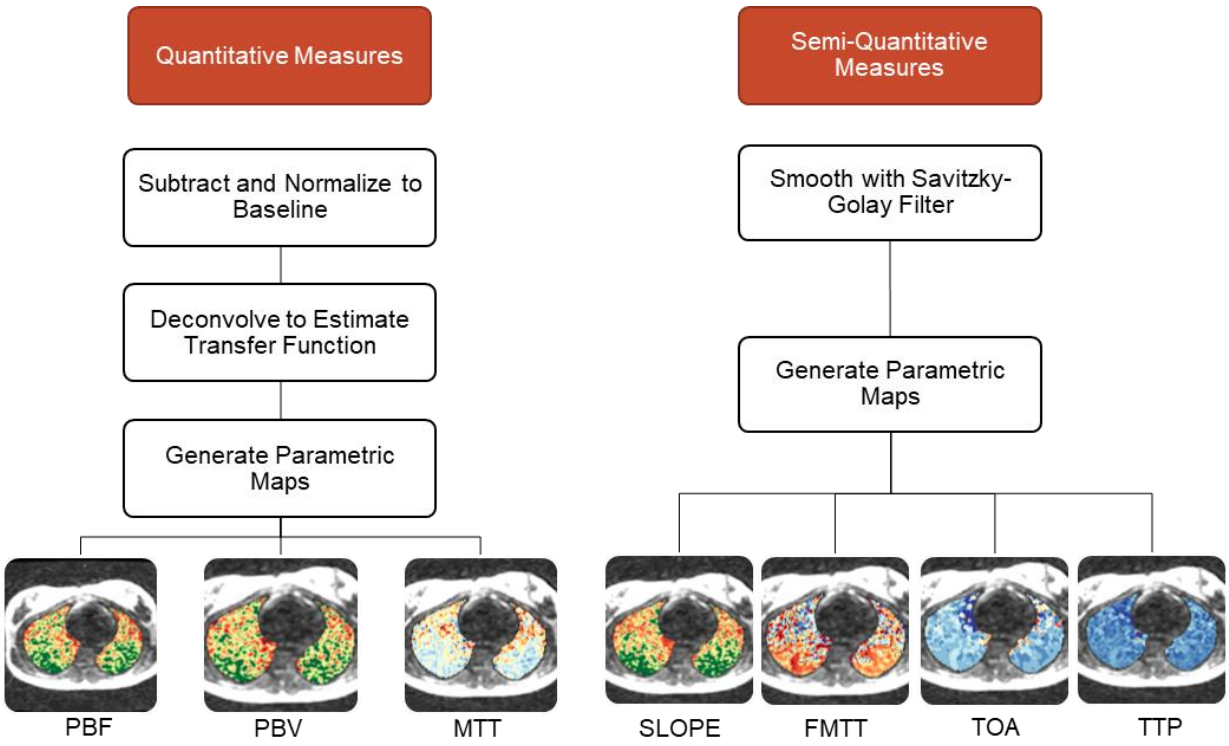

Supplemental Figure 3. Quantitative and semi-quantitative measurement computation workflow. Quantitative measures (left) are computed by first normalizing the signal intensity to the baseline mask signal. We then solve an ill-posed regularized least squares deconvolution problem and compute voxel wise parametric maps of pulmonary blood flow (PBF), pulmonary blood volume (PBV), and mean transit time (MTT). For the semi-quantitative measures, we first smooth each contrast enhancement time-series. A straightforward, noise robust calculation is then possible for SLOPE, FMTT, TOA, and TTP. For this work, perfusion related measurements will be displayed in a green/red colormap, while transit time related measurements will be displayed in blue/red measurements.

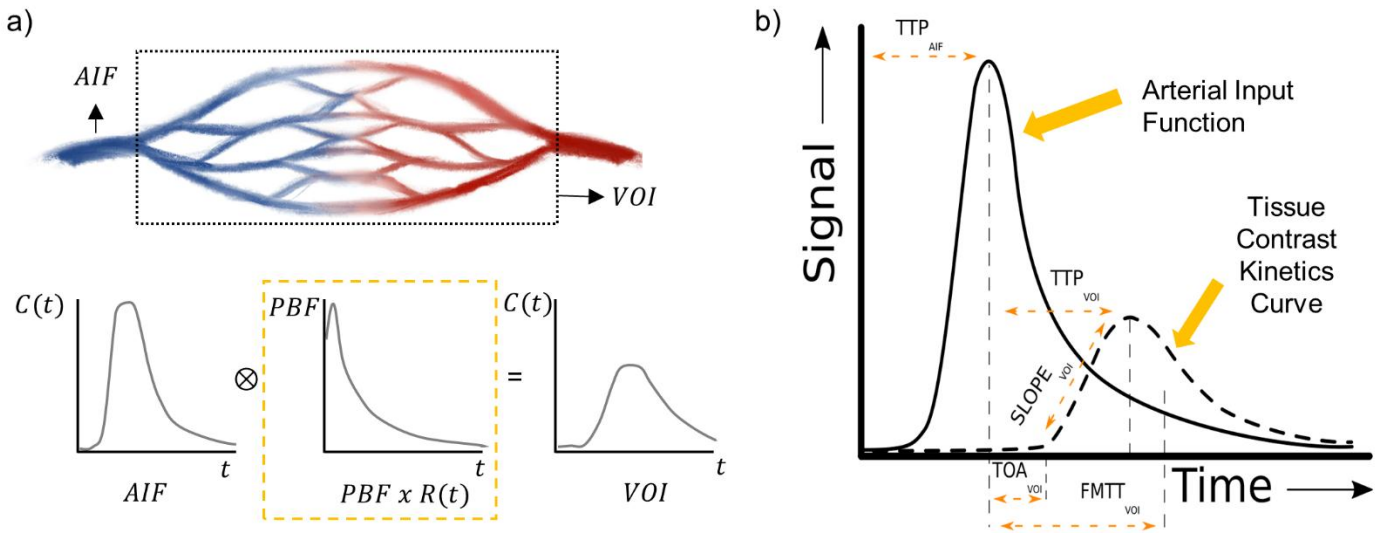

Supplementary Figure 4: Parameter computation visualization for a volume of interest (VOI). (a) Quantitative parameters are computed by deconvolving the arterial input function (*AIF*) from the tissue contrast kinetics (*C(t)*) to solve for the tissue residue function *R(t)*. With *R(t)* we can use algebra and the central volume theorem to solve for pulmonary blood flow (PBF), pulmonary blood volume(PBV), and mean transit time(MTT). (b) Semi-quantitative parameters time to peak(TTP), contrast uptake slope (SLOPE), time of arrival(TOA), and first moment transit time(FMTT) are computed from the contrast curve time-series itself, relative to the AIF time to peak (b).

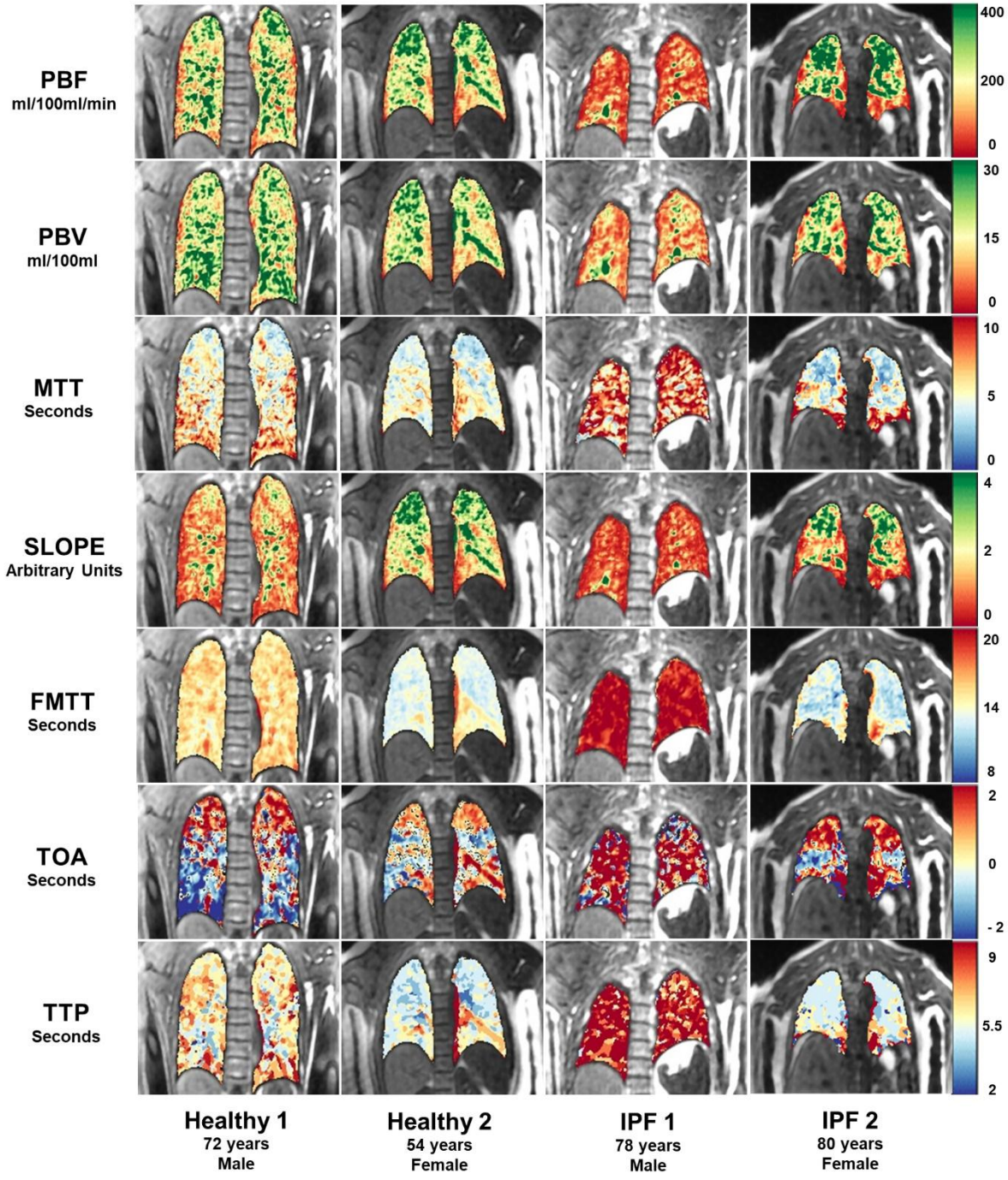

Supplementary Figure 5: Parameter map visualization. For flow related parameters, green and red colors indicate more and less perfusion, respectively. For transit time measures, blue and red indicate faster and slower transit times, respectively. Whole lung and regional abnormalities in are observed in idiopathic pulmonary fibrosis subjects relative to healthy control subjects. Significant spatial heterogeneity is observed in both cohorts. In IPF subjects inter-patient and regional spatial variations in severity of perfusion abnormalities were typically stronger relative to healthy subjects. For example, in IPF subject 1 reduced global perfusion and increased transit times were observed relative to healthy subjects 1 and 2, while in IPF subject 2 regional variation in each measure between the apical and basal lung regions are more prominent compared to healthy subjects 1 and 2.